

Ghost Imaging of Space Objects

Dmitry V. Strekalov,* Baris I. Erkmen,* and Nan Yu*

ABSTRACT. — The term “ghost imaging” was coined in 1995 when an optical correlation measurement using biphoton light from a parametric downconversion crystal was used to reconstruct an image of a mask by raster-scanning a detector in an empty optical channel. The ability to image objects nonlocally using only a “bucket” detector in the object channel and placing all high-resolution optics in the empty reference channel was found appealing by many scientists. The most important steps towards making this technique practical were understanding that thermal light sources can be used instead of biphoton sources, and that a bucket detector placed immediately after the object can be replaced by a distant point-like detector. We investigate the possibility of the next step, which would be to remove the optical beam splitter, which so far has been an indispensable part of ghost imaging with thermal light. In our approach, the object itself takes on the function of the beam splitter. If successful, this approach will allow for real-world application of the correlation imaging technique, even for the astronomical observations.

I. Why Ghost Imaging in Space? Motivation and History

Direct intensity measurement, by an eye or by a detector, has always been the foundation of observation astronomy. Sometimes this technique is successfully complemented by other types of measurements; for example, those relying on intensity correlations. The first and perhaps the most famous example of intensity interferometry applied in astronomy is the measurement of the angular size of a star by R. Hanbury Brown and R. Q. Twiss in 1957 [1]. The intensity correlation technique remains powerful and efficient to date. Fifty years after the pioneering work, a space-deployable version of this approach has been suggested [2].

A very different area of science from astronomy actively utilizing intensity correlations as a measurement tool is quantum optics. In particular, photon coincidence measurements have allowed for the study of nonclassical optical fields whose photons are emitted as tightly correlated pairs; e.g., in a process of parametric downconversion. Parametrically produced photons are not only tightly correlated in time, but also in space. This spatial correlation can predict the detectable “location” of one photon based on the observation of the other with a better resolution than a direct-intensity measurement. This fact has led to the idea of

* Communications Architectures and Research Section.

The research described in this publication was carried out by the Jet Propulsion Laboratory, California Institute of Technology, under a contract with the National Aeronautics and Space Administration. © 2013 California Institute of Technology. U.S. Government sponsorship acknowledged.

ghost imaging, which was first experimentally realized in 1995 [3]. The term “ghost imaging” describes a correlation measurement when the object’s image (or diffraction pattern [4]) is observed in the empty reference channel by a gated photon counting. The gating is obtained by photon detections in the object channel, which lacks any spatial resolution, as illustrated in Figure 1.

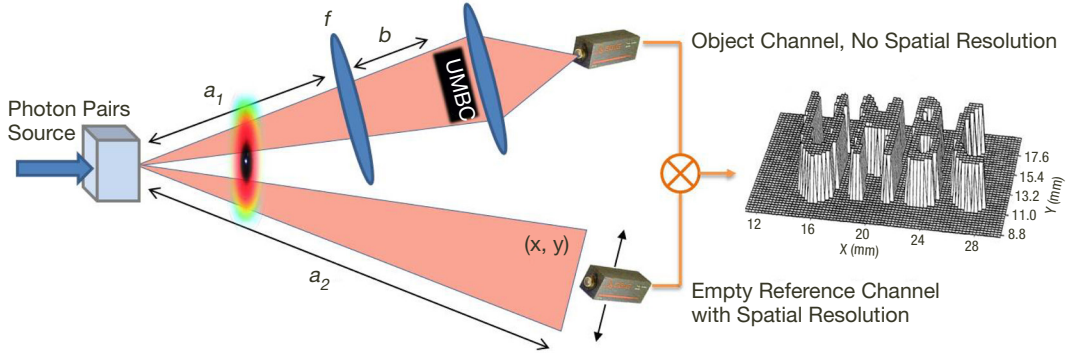


Figure 1. Simplified illustration of the original ghost imaging experiment [3]. A mask with letters “UMBC” is placed in the object channel, where all light is collected by a “bucket” detector. Nonetheless, an image is reconstructed by correlating this detector’s photon counts with those from another detector, raster-scanning the *empty* reference channel. A sharp image is observed when a modified thin lens equation is fulfilled: $1/(a_1 + a_2) + 1/b = 1/f$.

Besides its significance for the field of quantum optics, the ghost imaging technique has a few apparent practical advantages. Since no spatial resolution in the object channel is required, a very primitive single-pixel optical sensor could be placed in this channel, with the more advanced optics responsible for the image quality placed in the reference channel. This could be convenient for imaging of hard-to-access objects. The ghost imaging is especially beneficial for imaging the objects at “inconvenient” wavelengths, such as far-infrared, while the reference channel wavelength is visible [5]. Furthermore, the coincidence measurement technique is more robust in the presence of the optical background illumination. Finally, the possibility of surpassing the diffraction limit in ghost imaging has been discussed. However, here one should be careful to acknowledge that while the transverse intensity correlation of parametric photons is not constrained by the signal or idler wavelength diffraction, it is constrained by the pump wavelength diffraction.

Despite the apparent potential advantages, the first realization of ghost imaging was extremely far from any practical applications, and especially from astronomy. Indeed, the need for a laser-pumped source of photon pairs and the requirement to collect all light in the object channel (which means that the object has to be placed immediately before the collection optics) effectively ruled out such applications in astronomy or space physics.

Ten years after the initial ghost imaging demonstration, it was shown that the two-photon correlation properties of common thermal light are applicable for ghost imaging [6–8]. This may be considered as a first step towards ghost imaging in space. Since thermal light sources are much more abundant than parametric light sources, and in particular in space, this step was very important. Next, it was shown that collecting all the light in the object channel (the bucket detection) is not required and some portion of scattered light could be collected

instead [9]. This has allowed the object to be placed at a large distance from the observer. However, using a thermal light source brings about a new complication: a beam splitter that has to be placed between the source and the object. This beam splitter is needed to create the reference channel, whose speckle pattern duplicates that in the object channel, enabling the intensity correlation imaging. Such a geometry can be easily implemented in a lab, but becomes problematic when both the source and object are located far in space.

In this article, we investigate the possibility of ghost imaging in space by addressing the beam splitter issue. Our approach is illustrated in Figure 2. The underlying idea of our approach is that an object that partially transmits and partially reflects or scatters light can itself play the role of the beam splitter. Moreover, even a perfectly opaque (but not black) scattering object may under certain conditions (as discussed below) create coherence between the transmitted and scattered light, which may be utilized for the intensity correlation imaging. Since the object is present in both channels, this approach leads us away from “canonical” ghost imaging towards intensity interferometry of Hanbury Brown–Twiss type. The analogy and distinctions between these two types of imaging have been discussed in literature [10]. In our case, an important distinction is that we are not concerned with the angular size or other properties of the source, which will be assumed to be known. Instead, we will study the effect of the object’s geometry and location relative to the source and observer on the intensity correlation. We will attempt to restore these parameters from the correlation measurements and show that these results could provide important information in addition to conventional direct observations.

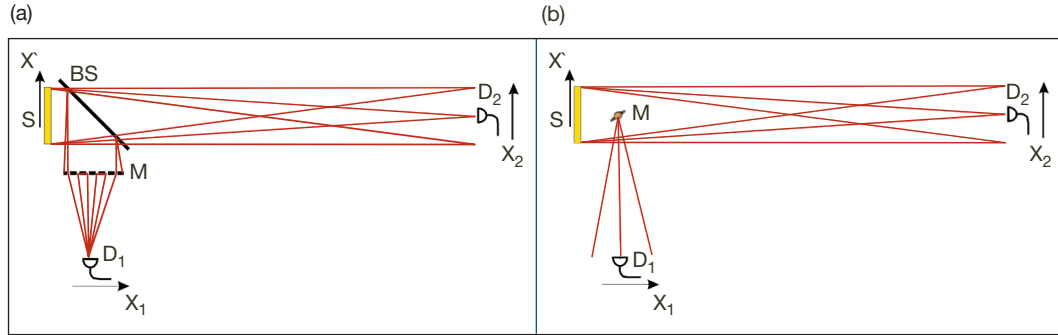


Figure 2. (a) Conceptual schematic of conventional thermal light ghost imaging setup, and (b) of our approach. S is a thermal light source, M is the object, $D_{1,2}$ are detectors, and BS (not present in case [b]) is a beam splitter.

In addition to the configuration shown in Figure 2(b), we will consider the case when both detectors receive transmitted and scattered light. This case is more realistic when both observers are ground-based and the distant source and object cannot be optically resolved.

In the following, we will develop and test a simple analytical model that will allow us to study the intensity correlation signatures of the simplest test objects. Based on this model, we will make predictions concerning the observability of various space objects and concerning their parameters that can be inferred from such observations. Potential space objects of interest will include Earth-like planets (including those near bright stars), gravitational lenses formed by black holes or other massive objects, dust, or gas clouds.

The rest of this article is organized as follows. In Section II, we will discuss the simplified geometry of the physical system under study and introduce its physical model. In Section III, we will narrow this model to a particular but very important case of equal distances from the object to the detectors. This will allow us to carry out this analysis in the analytical form and gain the insight into its physical aspects by considering two simple model objects. We will also test some of our theory predictions by comparing them to the actual astronomy observation data, available from the Kepler mission. In Section IV, we briefly discuss the consequences of departing from the equal arms limit. In Section V, we will discuss the signal-to-noise ratio (SNR) in the correlation measurement and compare it to a direct intensity measurement. The results of our analysis will be summarized in Section VI.

II. 2D Source and Object Model in Paraxial Approximation

Let us consider a flat source and a flat object placed in the source and object planes where we introduce the local transverse coordinates $\vec{\rho}$ and $\vec{\rho}_o$, respectively. Let L_s be the distance between the source and object planes, and $L_{1,2}$ the distances between the object plane and the planes of point-like detectors 1 and 2. The local transverse positions of these detectors are $\vec{\rho}_1$ and $\vec{\rho}_2$, respectively, as shown in Figure 3.

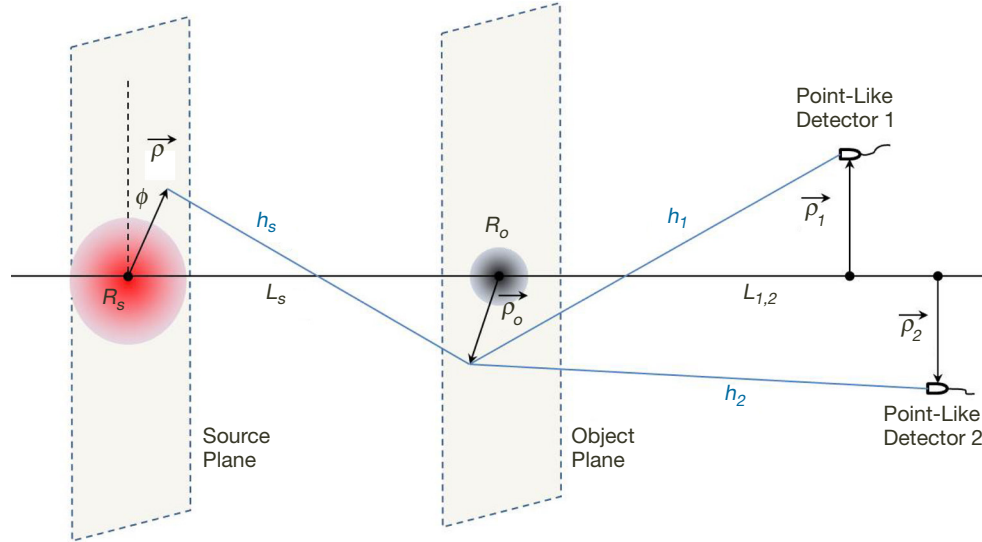


Figure 3. Relative position of the source, object, and detectors in the flat paraxial model.

Let us assume that the source field is bound by a Gaussian envelope with the width R_s and can be written as $E(\vec{\rho}, t) e^{-\frac{\rho^2}{2R_s^2}}$. This model approximates the source with a diameter (intensity distribution full width at half maximum [FWHM]) equal to $\sqrt{2}R_s$. In the paraxial approximation, the field at detector 1 is related to the field of the source as the following:

$$E_{1,2}(\vec{\rho}_1, t) = \iint d^2\rho d^2\rho_o e^{-\frac{\rho^2}{2R_s^2}} E(\vec{\rho}, t - \frac{L_1 + L_s}{c}) h_{L_s}(\vec{\rho} - \vec{\rho}_o) T(\vec{\rho}_o) h_{L_{1,2}}(\vec{\rho}_o - \vec{\rho}_{1,2}). \quad (1)$$

Although it looks complicated, Equation (1) is actually quite straightforward. It takes advantage of the field propagation functions

$$h_Z(\vec{x}) = \frac{e^{ikZ}}{i\lambda Z} e^{ik\frac{|\vec{x}|^2}{2Z}} \quad (2)$$

relating the electric field at two spatial points separated by a distance Z in one direction and by a transverse displacement \vec{x} (assuming that $x \ll Z$; i.e., the paraxial approximation) in the transverse directions. A field produced by an extended source in a remote point is then given by a convolution of Equation (2) with the source's own field distribution. This procedure yields the field distribution across the object. We multiply this by the object's transmission function $T(\vec{\rho}_o)$, which may be real (purely absorbing object), imaginary (purely phase object; e.g., a thin lens) or complex. Then we repeat the propagation and integration steps to obtain Equation (1), which is the field at the detector. A relation similar to Equation (1) can be written for the field at the other detector.

Let us consider the correlation-based ghost imaging. In this case, the observable is

$$\langle I_1(\vec{\rho}_1, t_1) I_2(\vec{\rho}_2, t_2) \rangle \propto \langle E_1^\dagger(\vec{\rho}_1, t_1) E_2^\dagger(\vec{\rho}_2, t_2) E_1(\vec{\rho}_1, t_1) E_2(\vec{\rho}_2, t_2) \rangle, \quad (3)$$

where the fields can be treated as quantum-mechanical operators, or as classical values. For thermal light, the phase-sensitive term in Equation (3) vanishes [11], and we arrive at

$$\langle I_1(\vec{\rho}_1, t_1) I_2(\vec{\rho}_2, t_2) \rangle \propto |\langle E_1^\dagger(\vec{\rho}_1, t_1) E_2(\vec{\rho}_2, t_2) \rangle|^2 + \langle E_1^\dagger(\vec{\rho}_1, t_1) E_1(\vec{\rho}_1, t_1) \rangle \langle E_2^\dagger(\vec{\rho}_2, t_2) E_2(\vec{\rho}_2, t_2) \rangle, \quad (4)$$

where the first term describes the possible ghost image and the second term gives the uncorrelated “background” intensity product, which also describes the object's shadow. To separate these effects, it is convenient to introduce the normalized Glauber correlation function [12]

$$g^{(2)}(\vec{\rho}_1, t_1; \vec{\rho}_2, t_2) = 1 + \frac{|\langle E_1^\dagger(\vec{\rho}_1, t_1) E_2(\vec{\rho}_2, t_2) \rangle|^2}{\langle E_1^\dagger(\vec{\rho}_1, t_1) E_1(\vec{\rho}_1, t_1) \rangle \langle E_2^\dagger(\vec{\rho}_2, t_2) E_2(\vec{\rho}_2, t_2) \rangle} = 1 + \frac{|G_{12}|^2}{G_{11} G_{22}}. \quad (5)$$

The Glauber correlation function will be our main observable in the following treatment. However, let us mention that other types of measurements are possible. In particular, one can measure higher-order correlation functions $g^{(m,n)}$, or the variance of intensity difference (rather than a product) [13–15]. The analysis based on the field propagation equation, Equation (1), can be easily extended to these measurements. Such measurements will have different dependencies on the optical mode structure and on the detector's quantum efficiencies, and may offer interesting resolution–SNR trade-off opportunities. The possibility of utilizing these measurement strategies distinguishes our approach from the conventional intensity interferometry.

Substituting the fields $E_1(\vec{\rho}_1, t_1)$ and $E_2(\vec{\rho}_2, t_2)$ given by Equation (1) into Equation (5), we take into account the correlation property of the source field $E(\vec{\rho}, t)$:

$$\langle E^\dagger(\vec{\rho}, t) E(\vec{\rho}', t') \rangle \propto \delta(\vec{\rho} - \vec{\rho}') \Gamma(t - t'), \quad (6)$$

where Γ is a δ -like function whose width corresponds to the optical coherence time. The latter may be determined by the spectral filters bandwidth. Unless we are interested in color imaging, using narrow-band filters is undesirable because they reduce the signal. On the other hand, short coherence time requires compatibly fast optical detectors and correlation circuitry, in order to ensure single longitudinal mode detection. Therefore, to carry out a fair comparison between the direct intensity measurement and the correlation measurement, we need to take into account the photon flux reduction due to the minimal spectral filtering, required in the latter case. Let us assume a 1-ps timing accuracy and the central wavelength of 1 micron. At this wavelength, the 1-ps coherence time corresponds to a 3.3-nm-wide spectral band. Comparing the optical power detected within this band to the total power within the typical band of a silicon photodetector (see Figure 4), we find that for a correlation measurement we have 0.5 percent of the power at our disposal than for the broadband intensity measurement. This reduces the SNR in a shot-noise-limited, narrow-band measurement. The relative SNR will be more favorable for the correlation measurement when compared to a color-resolved intensity measurement. In particular, no flux loss will be suffered if one is interested in a very narrow-band measurement; e.g., a measurement with a specific spectral line. A more detailed discussion of the direct intensity vs. correlation measurement SNRs will be given in Section V.

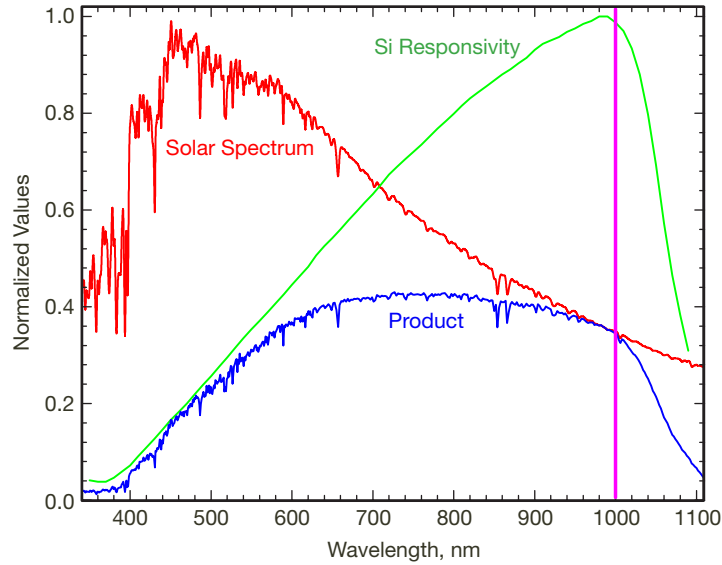


Figure 4. The solar radiation normalized spectral density (from [16]), spectral sensitivity of a typical silicon photodiode, and their product.

Let us point out that in addition to the high speed and low jitter requirements on the photodetectors and correlation electronics, the broadband correlation measurement placed stringent requirements on the clock synchronization between the two detectors, as well as on the knowledge of their relative position $L_1 - L_2$.

To continue our analysis, we will assume that perfect synchronization between the detectors has been achieved and $\Gamma(t - t') = 1$ in Equation (6). We then suppress the temporal part of the problem. For the numerator in Equation (5), we derive

$$G_{12}(\vec{\rho}_1, \vec{\rho}_2) = \int \int \int d^2 \rho d^2 \rho'_o d^2 \rho_o e^{-\frac{\rho^2}{R_s^2}} T_2(\vec{\rho}_o) T_1^*(\vec{\rho}'_o) h_{L_s}^*(\vec{\rho} - \vec{\rho}'_o) h_{L_s}(\vec{\rho} - \vec{\rho}_o) h_{L_1}^*(\vec{\rho}'_o - \vec{\rho}_1) h_{L_2}(\vec{\rho}_o - \vec{\rho}_2). \quad (7)$$

In Equation (7), we have introduced $T_{1,2}(\vec{\rho}_o)$ to allow the transmission functions to be different for detectors 1 and 2. This will allow us to consider the scenario when the object (partially) obscures the light source for one detector, and scatters it to the other. That is, the former detector receives the direct light from the source, but the latter only sees the light scattered by the object. In handling such situations, we still need to make sure the paraxial approximation holds, and that the approximation of a flat object remains reasonable.

For the following analysis, it will be convenient to introduce a correlation function

$$G_{12}^{(R_s)}(Z_a, \vec{\rho}_a; Z_b, \vec{\rho}_b) = \int d^2 \rho e^{-\frac{\rho^2}{R_s^2}} h_{Z_a}^*(\vec{\rho} - \vec{\rho}_a) h_{Z_b}(\vec{\rho} - \vec{\rho}_b) \quad (8)$$

for the fields emitted by an extended Gaussian source of thermal light that has a width R_s and is located at $Z = 0$, propagating to locations $(Z_a, \vec{\rho}_a)$ and $(Z_b, \vec{\rho}_b)$. Equivalently, from the *advanced wave* perspective [17–19], it describes time-reversed propagation of a photon from $(-Z_a, \vec{\rho}_a)$ to the source, and then forward in time to $(Z_b, \vec{\rho}_b)$. If the source is infinitely large, $R_s \rightarrow \infty$, the aperture-limited propagation function, Equation (8), becomes equal to a point-source propagation function from one detector to the other:

$$G_{12}^{(\infty)}(Z_a, \vec{\rho}_a; Z_b, \vec{\rho}_b) = h_{Z_b - Z_a}(\vec{\rho}_b - \vec{\rho}_a). \quad (9)$$

The two-point propagation function arises in Equation (5):

$$G_{12}(\vec{\rho}_1, \vec{\rho}_2) = \int \int d^2 \rho_o d^2 \rho'_o h_{L_2}(\vec{\rho}_o - \vec{\rho}_2) h_{L_1}^*(\vec{\rho}'_o - \vec{\rho}_1) T_2(\vec{\rho}_o) T_1^*(\vec{\rho}'_o) G_{12}^{(R_s)}(L_s, \vec{\rho}'_o; L_s, \vec{\rho}_o), \quad (10)$$

and likewise for $G_{11}(\vec{\rho}_1)$ and $G_{22}(\vec{\rho}_2)$. To evaluate $G_{12}^{(R_s)}(Z_a, \vec{\rho}_a; Z_b, \vec{\rho}_b)$ in a general form, we introduce polar coordinates such that

$$\int d^2 \rho = \int_0^\infty \rho d\rho \int_0^{2\pi} d\varphi, \quad |\vec{\rho}_a - \vec{\rho}_b|^2 = \rho_a^2 + \rho_b^2 - 2\rho_a \rho_b \cos(\varphi_a - \varphi_b). \quad (11)$$

The angular integration in Equation (8) yields

$$G_{12}^{(R_s)}(Z_a, \vec{\rho}_a; Z_b, \vec{\rho}_b) = 2\pi \frac{e^{ik(Z_b - Z_a)}}{\lambda^2 Z_a Z_b} e^{i\frac{k}{2}(\rho_b^2/Z_b - \rho_a^2/Z_a)} \int_0^\infty \rho d\rho e^{-\rho^2 \left[\frac{1}{R_s^2} + ik \frac{Z_b - Z_a}{2Z_a Z_b} \right]} J_0 \left(k\rho \left| \frac{\vec{\rho}_b}{Z_b} - \frac{\vec{\rho}_a}{Z_a} \right| \right). \quad (12)$$

Then integrating over the radius, we obtain

$$G_{12}^{(R_s)}(Z_a, \vec{\rho}_a; Z_b, \vec{\rho}_b) = 2\pi \frac{R_s^2}{\lambda^2} \frac{e^{ik(Z_b - Z_a)}}{2Z_a Z_b + ikR_s^2(Z_b - Z_a)} e^{i\frac{k}{2}(\rho_b^2/Z_b - \rho_a^2/Z_a)} e^{-\frac{k^2}{2} \left| \frac{\vec{\rho}_b}{Z_b} - \frac{\vec{\rho}_a}{Z_a} \right|^2} \frac{R_s^2 Z_a Z_b}{2Z_a Z_b + ikR_s^2(Z_b - Z_a)}. \quad (13)$$

In the case of interest, Equation (10), we have $Z_a = Z_b = L_s$, which leads to

$$G_{12}^{(R_s)}(L_s, \vec{\rho}_o'; L_s, \vec{\rho}_o) = q^2 \pi^{-1} e^{i \frac{q}{R_s} (\rho_o^2 - \rho_o'^2)} e^{-q^2 |\vec{\rho}_o - \vec{\rho}_o'|^2}, \quad (14)$$

where $q^{-1} = 2L_s / (kR_s)$ is the speckle size.

III. Balanced Arms Configuration

In this section, we consider the special balanced case when $L_1 = L_2 = L$. While this case limits the possible observation scenario, it allows us to carry out exact analytical calculations in many cases of interest, and to assess the practical utility of our approach. To carry out these calculations, it will be convenient to introduce the new coordinates $\vec{x} = (\vec{\rho}_o + \vec{\rho}_o') / \sqrt{2}$ and $\vec{y} = (\vec{\rho}_o - \vec{\rho}_o') / \sqrt{2}$. Then substituting Equation (14) into Equation (10), we obtain

$$G_{12}(\vec{\rho}_1, \vec{\rho}_2) = A \int \int S(\vec{x}, \vec{y}) e^{-2q^2 y^2} e^{i \vec{\Delta} \cdot \vec{x}} e^{i \vec{\Sigma} \cdot \vec{y}} e^{i \gamma \vec{x} \cdot \vec{y}} d^2 x d^2 y, \quad (15)$$

where

$$\begin{aligned} A &= \pi \left(\frac{R_s}{\lambda^2 L L_s} \right)^2 e^{\frac{ik}{2L} (\rho_2^2 - \rho_1^2)}, \\ S(\vec{x}, \vec{y}) &= T_2 \left(\frac{\vec{x} + \vec{y}}{\sqrt{2}} \right) T_1^* \left(\frac{\vec{x} - \vec{y}}{\sqrt{2}} \right), \\ \vec{\Delta} &= \frac{k}{\sqrt{2} L} (\vec{\rho}_1 - \vec{\rho}_2), \\ \vec{\Sigma} &= \frac{k}{\sqrt{2} L} (\vec{\rho}_1 + \vec{\rho}_2), \\ \gamma &= k(1/L + 1/L_s). \end{aligned} \quad (16)$$

The Gaussian term in Equation (15) arises from Fourier transform of the source field distribution. This suggests that Equation (15) could be generalized for any such distribution. However, at this stage we will limit our consideration to a Gaussian source.

As a sanity check, we notice that if we “turn off” the object by setting $S(\vec{x}, \vec{y}) = 1$, the integral over $d^2 x$ in Equation (15) yields $(2\pi)^2 \delta(\vec{\Delta} + \gamma \vec{y})$. Then the $d^2 y$ integral yields, quite expectedly, the correlation function of a Gaussian source, Equation (14), with increased free-space propagation length $L_s \rightarrow L + L_s$:

$$G_{12}(\vec{\rho}_1, \vec{\rho}_2) \rightarrow G_{12}^{(R_s)}(L + L_s, \vec{\rho}_1; L + L_s, \vec{\rho}_2). \quad (17)$$

Let us now consider a few example objects and discuss their possible relevance for the astronomy applications.

A. A Gaussian Absorber

This case can represent, e.g., a spherical dust or gas cloud of roughly uniform density. It also can be used as a crude model for a planet occluding a star. The transmission function of such an object can be modeled as

$$T(\vec{\rho}_o) = 1 - T_0 e^{-\frac{\rho_o^2}{2R_o^2}}, \quad (18)$$

which gives rise to four terms:

$$S(\vec{x}, \vec{y}) = S_0 + S_{1a} + S_{1b} + S_2 = 1 - T_0 e^{-\frac{(\vec{x} + \vec{y})^2}{4R_o^2}} - T_0 e^{-\frac{(\vec{x} - \vec{y})^2}{4R_o^2}} + T_0^2 e^{-\frac{x^2 + y^2}{2R_o^2}}. \quad (19)$$

In Equations (18) and (19), T_0 is the amplitude transmission of the most opaque (central) part of the object. Consequently, the correlation function also will consist of four terms: $G_{12} = G_{12}^{(0)} + G_{12}^{(1a)} + G_{12}^{(1b)} + G_{12}^{(2)}$, where the zero-order term corresponds to free-space propagation, Equation (17): $G_{12}^{(0)} = G_{12}^{(R_s)}(L + L_s, \vec{\rho}_1; L + L_s, \vec{\rho}_2)$. A straightforward but cumbersome calculation gives both the first- and the second-order terms in the form

$$G_{12}^{(1,2)}(\vec{\rho}_1, \vec{\rho}_2) = \frac{(-T_0)^n}{\pi(\tilde{q}^2 + R_o^2 \tilde{\gamma}^2)} \left(\frac{k^2 R_s R_o}{2LL_s} \right)^2 e^{-i \frac{k^2 R_o^2 \tilde{\gamma}}{2L^2} \frac{\rho_2^2 - \rho_1^2}{\tilde{q}^2 + R_o^2 \tilde{\gamma}^2}} e^{-\frac{k^2(\vec{\rho}_2 + \vec{\rho}_1)^2}{8L^2(\tilde{q}^2 + R_o^2 \tilde{\gamma}^2)}} e^{-\frac{k^2 R_o^2 \tilde{q}^2 (\vec{\rho}_2 - \vec{\rho}_1)^2}{2L^2 \tilde{q}^2 + R_o^2 \tilde{\gamma}^2}}. \quad (20)$$

To obtain $G_{12}^{(1a,b)}$, we substitute in Equation (20)

$$n = 1, \quad \tilde{q}^2 = 2q^2 + \frac{1}{4R_o^2}, \quad \tilde{\gamma} = \gamma \pm \frac{i}{2R_o^2}.$$

For $G_{12}^{(2)}$, we substitute

$$n = 2, \quad \tilde{q}^2 = 2q^2 + \frac{1}{2R_o^2}, \quad \tilde{\gamma} = \gamma.$$

We notice that in the multimode case when the speckle size on the object greatly exceeds the object size, $\tilde{q}^2 \approx 2q^2$. However, we do not need to make this approximation now.

First, let us investigate the result, Equation (20), for a set of parameters that can be easily implemented in a table-top experiment. In Figure 5, we show a correlation function $g^{(2)}(\vec{\rho}_1 = -\vec{\rho}_2)$ in Figure 5(a) and the intensity profile featuring the object's shadow in Figure 5(b). In this simulation, the opaque ($T_0 = 1$) object is placed between the source ($R_s = 1$) and the detector plane so that $L_s = L = 50$ cm. The object size R_o is varied from zero to 1, 2, and 3 mm. As the object becomes larger, its shadow becomes deeper and (less intuitively) the speckle size becomes smaller. For larger objects, the speckle shape also becomes distorted. Even less intuitive, evolution is undergone by the speckle size as the object is moved across the line of sight imitating a planet passing across the star. The speckle first gets broader, and then narrower, reaching the minimum when the object is exactly on the line of sight (see Figure 6). To simulate this transient, we actually changed the detector's position $\rho_d = (\rho_1 + \rho_2)/2$ while the $R_o = 1$ mm object was fixed on the initial line of sight at $L_s = L = 50$ cm. The effective displacement of the object from the line of sight was

then found as $\rho_o = \rho_d L_s / (L + L_s)$. In Figure 6, we show the corresponding variation of the speckle width and of the intensity. Remarkably, the fractional variation of both values due to the transient object is approximately 7 percent.

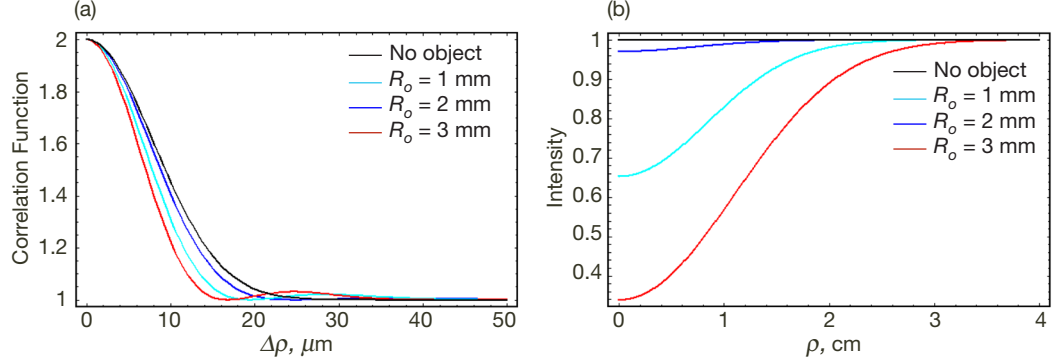


Figure 5. (a) The correlation function $g^{(2)}(\vec{\rho}_1, \vec{\rho}_2)$ versus the distance $\Delta\rho = |\vec{\rho}_1 - \vec{\rho}_2|$, and (b) the intensity profile for a lab parameter set ($T_0 = 1$, $L_s = L = 50\text{ cm}$, $R_s = 1\text{ cm}$). The object size R_o is varied from zero to 1, 2, and 3 mm.

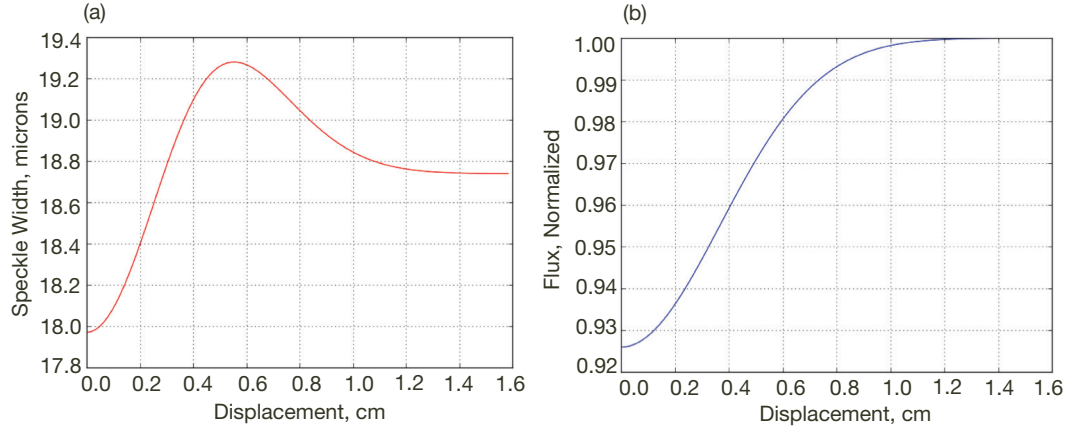


Figure 6. (a) Dependence of the correlation function $g^{(2)}(\Delta\rho)$ width, and (b) of the normalized photon flux on displacement of the object from the line of sight ρ_o , for a lab parameter set ($T_0 = 1$, $L_s = L = 50\text{ cm}$, $R_s = 1\text{ cm}$, $R_o = 1\text{ mm}$).

Let us now apply our model to an actual astronomical observation carried out by the Kepler space telescope [20,21]. Substituting in our model the Kepler-20f parameters [21], we find the relative intensity variation of the order of 10^{-4} , which is consistent with the actual observation [21] (see Figure 7). In line with the earlier discussion, we use the planet radius times $\sqrt{2}$ as R_o . The disagreement in the dip shape arises from using the Gaussian absorber model while the actual planet is, of course, better described by an opaque disk. However, the numerical agreement with the experiment shows that even a simplistic, fully analytical Gaussian model can be useful. Following this model, we predict the variation of the speckle size from 3,604.0 m when the planet is out of the line of sight to 3,603.7 m when it is in the line of sight, which corresponds to the relative variation of 7.6×10^{-5} or, accounting for the off-axis speckle broadening, to approximately 1.4×10^{-4} . Again, the magnitude of this

variation is very close to the magnitude of the photon flux variation. Of course, a detailed SNR analysis is required in order to conclude which type of planetary detection will be more efficient. Let us, however, point out that the measurement of the speckle width does not preclude the conventional intensity measurement, such as has been carried out in the Kepler experiment, and can be considered as an extension of such a measurement rather than its substitute.

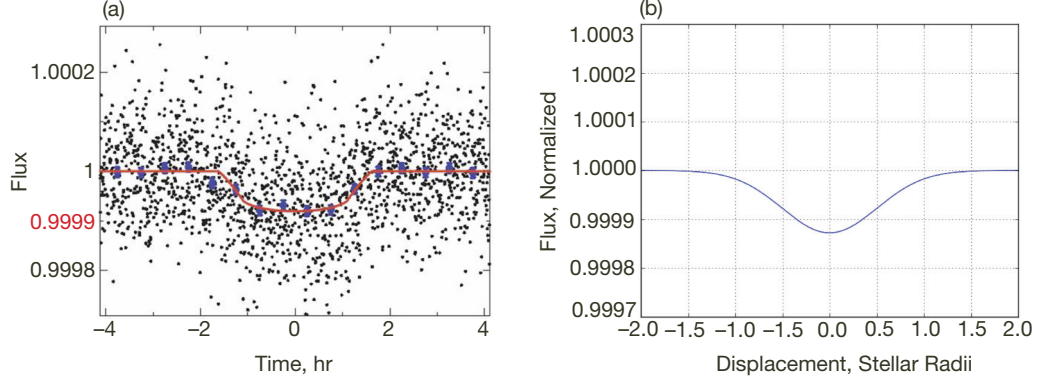


Figure 7. (a) The intensity variation for Kepler-20e observed in [21], and (b) computed based on our model.

B. Phase Objects

Let us consider another model object allowing for the fully analytical treatment: a thin lens. The motivation for studying this example is the possibility to observe a purely phase object where direct intensity measurements may not be as efficient as with opaque objects. Examples of such objects in space may be gravitational lenses or dilute gas clouds. For an infinite thin lens with focal distance f ,

$$S(\vec{x}, \vec{y}) = e^{-\frac{ik}{2f}(\rho_o^2 - \rho_s^2)} = e^{-i\frac{k}{f}\vec{x}\vec{y}}. \quad (21)$$

The effect of such a lens can be absorbed into $\gamma \rightarrow \gamma_f = k(1/L + 1/L_s - 1/f)$, and we quickly arrive at

$$\begin{aligned} G_{11} = G_{22} &= \frac{q^2}{\pi D^2} = \text{const} |\tilde{\rho}_{1,2}|, \\ G_{12}(\tilde{\rho}_1, \tilde{\rho}_2) &= \frac{q^2}{\pi D^2} e^{\frac{ik}{2L} \frac{D-1}{D}(\rho_2^2 - \rho_1^2)} e^{-(q/D)^2 |\tilde{\rho}_2 - \tilde{\rho}_1|^2}, \\ g_{12}(\tilde{\rho}_1, \tilde{\rho}_2) &= 1 + e^{-2(q/D)^2 |\tilde{\rho}_2 - \tilde{\rho}_1|^2}, \end{aligned} \quad (22)$$

where $D \equiv L(1/L + 1/L_s - 1/f)$ is a dimensionless “out-of-focus” factor. If the lens images the source plane onto the detector plane, then $D = 0$ and the speckles become infinitely small while the intensity goes to infinity. The former is a consequence of our assumption, Equation (6), of a delta-correlated source field. The latter is a consequence of the paraxial approximation, as well as the coordinate-independent intensities in Equation (22). If the

source is in focus, then the light propagates as a collimated beam, $D = 1$, and the speckle size as well as the intensity in the detector plane will be the same as in the lens plane.

Let us consider another example of a combined phase and amplitude lens-like object. This object has a finite extent and allows for the analytical treatment. Its transmission function is

$$T(\vec{\rho}_o) = 1 - e^{-\frac{\rho_o^2}{2R_o^2}} \left(1 - e^{-\frac{ik\rho_o^2}{2f}}\right). \quad (23)$$

This object can produce shadows very similar to those from a Gaussian absorber — see Figures 8(a) and (b). Therefore, it would not be possible to distinguish these two objects based on the intensity measurement. However, the behavior of the speckle widths is clearly distinct, as we see from Figures 8(c) and (d) (notice the difference in the signal magnitude, as well as in its character). This direct example demonstrates the potential the correlation measurement has for the object *characterization*, beyond its mere detection.

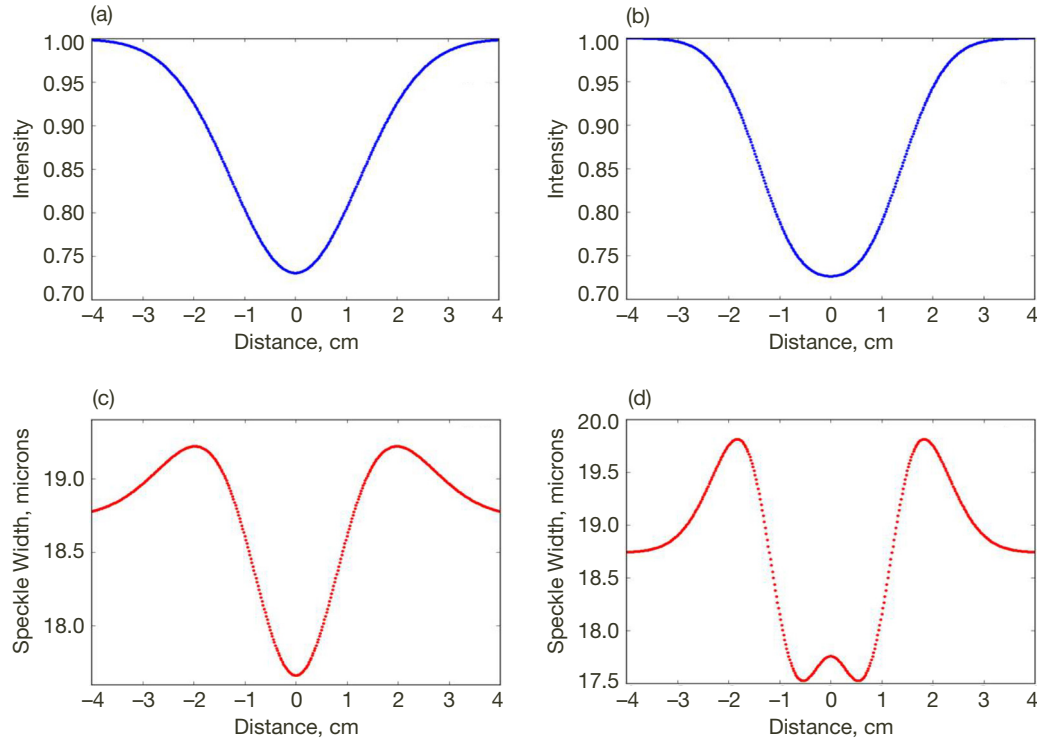


Figure 8. (a) A shadow from a test object, Equation (23), with $R_o = 3$ mm and $f = 1$ m inserted between the source and detectors as a function of its distance from the line of sight; (b) a shadow from a Gaussian absorber with $R_o = 5$ mm and $T_0 = 0.62$; (c) and (d) the speckle width for (a) and (b), respectively. In this simulation, $L_s = L_1 = L_2 = 50$ cm, $R_s = 1$ cm.

IV. Unbalanced Arms Configuration

In this section, we consider a more general case of $L_1 \neq L_2$, which may be important for an asymmetric configuration; e.g., when the correlation measurement is performed by a ground-based detector jointly with a distant space-based detector. We will continue to assume perfect time synchronization between the two detectors, or equivalently, a monochromatic light source. However, we will not be able to carry out the analytical calculations without making some reasonable approximations. From Equation (13), we see that the *large aperture approximation*, Equation (9), holds if

$$\alpha_s \equiv \frac{2Z_a Z_b}{kR_s^2 |Z_b - Z_a|} \ll 1. \quad (24)$$

This approximation is appropriate for evaluation of the first-order terms in Equation (10), where $Z_b - Z_a = L_1$ is large. Indeed, in this case, for the optics lab geometry $\lambda = 1 \mu\text{m}$ and $R_s = L_s = 1 \text{ cm}$, we get $\alpha_s = 1.6 \times 10^{-5}$. For the solar system geometry with $R_s = 7 \times 10^5 \text{ km}$ (Sun radius), $L_s = 1.5 \times 10^8 \text{ km}$ (the distance from Earth to the Sun), and $\lambda = 1 \mu\text{m}$, we get $\alpha_s = 5 \times 10^{-14}$. This parameter becomes even smaller for interstellar distances. Therefore, when we calculate G_{12} , Equation (10), for a Gaussian absorber described by Equation (18), the first-order terms can be approximated as

$$G_{12}^{(1)}(\vec{\rho}_1, \vec{\rho}_2) \equiv G_{12}^{(1a)}(L_1, \vec{\rho}_1; L_2, \vec{\rho}_2) + G_{12}^{(1b)*}(L_2, \vec{\rho}_2; L_1, \vec{\rho}_1) \approx -2 \int d^2 \rho e^{-\frac{\rho^2}{2R_o^2}} h_{L_1}^*(\vec{\rho} - \vec{\rho}_1) h_{L_2}(\vec{\rho} - \vec{\rho}_2). \quad (25)$$

The opposite case of Equation (24) occurs when $Z_a = Z_b$. If, furthermore, q^2 is much greater than all coefficients that multiply ρ^2 in all real and imaginary exponents in Equation (10), then Equation (14) can be proven to approach a δ -function normalized to unity. This is the *small-aperture approximation*, applicable for the second-order terms of Equation (10). Let us point out that within this approximation, the object cannot create coherence between the transmitted and scattered light unless the speckle size in the object plane approaches or exceeds the size of the object itself.

It is easy to see that for the optics lab geometry as described above, q^2 exceeds all relevant parameters by a factor of at least 3×10^4 . The excess factors are much greater in all reasonable astronomical geometries. Therefore, we derive

$$G_{12}^{(2)}(\vec{\rho}_1, \vec{\rho}_2) \approx \int d^2 \rho e^{-\frac{\rho^2}{R_o^2}} h_{L_1}^*(\vec{\rho} - \vec{\rho}_1) h_{L_2}(\vec{\rho} - \vec{\rho}_2). \quad (26)$$

Therefore, for a Gaussian absorber case with $L_1 \neq L_2$, we have the following approximate expressions:

$$\begin{aligned} G_{12}^{(0)}(\vec{\rho}_1, \vec{\rho}_2) &= G_{12}^{(R_s)}(L_1 + L_s, \vec{\rho}_1; L_2 + L_s, \vec{\rho}_2), \\ G_{12}^{(1)}(\vec{\rho}_1, \vec{\rho}_2) &= -2G_{12}^{(\sqrt{2}R_o)}(L_1, \vec{\rho}_1; L_2, \vec{\rho}_2), \\ G_{12}^{(2)}(\vec{\rho}_1, \vec{\rho}_2) &= G_{12}^{(R_o)}(L_1, \vec{\rho}_1; L_2, \vec{\rho}_2). \end{aligned} \quad (27)$$

Let us first evaluate the correlation function $g^{(2)}$ found by substituting Equation (27) into Equation (5) in the absence of the object, by setting $R_o = 0$. In Figure 9(a), we show this function for typical optical lab parameters ($L_1 = 55$ cm, $L_2 = L_1 + \Delta L$, $L_s = 55$ cm, $\lambda = 1$ μ m), where we assumed that the detectors are coplanar with the line of sight and lie on its opposite sides: $\vec{\rho}_1 = -\vec{\rho}_2$. This allows us to use a single scalar parameter, $\Delta\rho$, in the same way it was done in Figure 5.

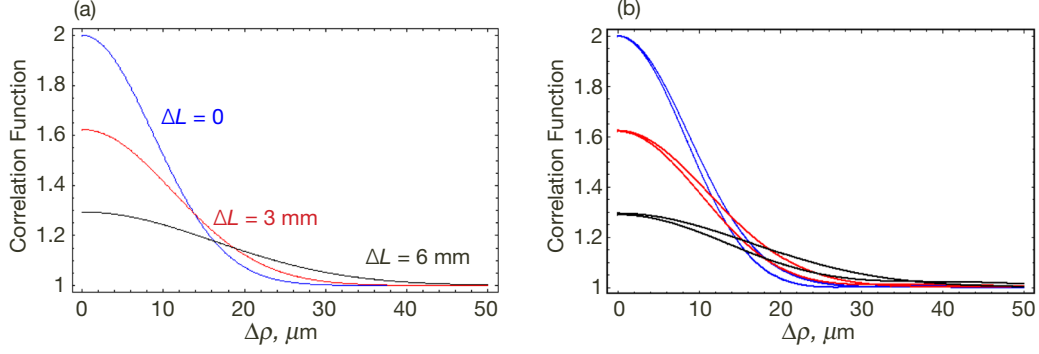


Figure 9. (a) The correlation functions $g^{(2)}(\Delta\rho)$ in the absence of an object for $R_s = 1$ cm, $L_1 = 55$ cm, and $L_2 = L_1 + \Delta L$; (b) the same correlation functions (solid lines) become narrower (dashed lines) when a small ($R_o = 1$ mm) Gaussian absorbing object is inserted in the line of sight at the distance $L_s = 55$ cm from the source.

The correlation loss due to ΔL is clearly visible. We would like to emphasize that this is not due to a limited longitudinal coherence of the source, but because of its transverse coherence properties. We can interpret this result as follows. By placing the first detector in the plane L_1 , we define the speckle pattern in this plane as the transverse mode structure. These speckles may be further considered as mutually incoherent light sources. As light from these sources propagates further, the coherence areas expand as well as overlap. The expansion causes the widening of the correlation function while the overlap causes the contrast reduction due to multimode detection. Using the expression $g^{(2)}(0) = 1 + 1/m$ relating the correlation peak for thermal light to the number of detected modes m , we can determine that in our example the longitudinal displacement of the detector by $\Delta L = 6$ mm has led to the number of detected modes $m \approx 3$. Note that this interpretation differs from the speckle pattern behavior that one might observe, e.g., on a screen. In this case, the speckles do not overlap and do not appreciably change in size for small longitudinal translations.

Now let us “turn on” the object and investigate its effect on the correlation function. If a small ($R_o = 1$ mm) object is placed halfway between the source and the detectors, the correlation function becomes narrower, which means smaller speckles — see Figure 9(b).

Let us point out that the $\Delta L = 0$ case in Figure 9 is consistent with the $R_o = 1$ mm case from Figure 5, which validates the large-aperture and small-aperture approximations for an absorbing object. On the other hand, we notice that it fails for a phase object such as a thin large lens. When the small-aperture approximation is utilized and Equation (14) is treated as a δ -function, such object is “erased” by taking the absolute-square of $T(\rho_o)$.

V. Signal-to-Noise Ratio Analysis

The sensitivity of the correlation-based measurements can be ascertained by a careful study of the SNR, which strongly depends on the object of interest and the imaging geometry. As a result, the value added by the correlation-based measurement can range from significant to negligible. The quantitative analysis of the SNR for both types of measurements can leverage SNR calculations for Hanbury Brown–Twiss intensity interferometry, because performing ghost imaging at intergalactic scales often yields geometries wherein the detectors are point-like (rather than bucket-like, which is more common in lab demonstrations of ghost imaging).

The ghost imaging configuration shown in Figure 3 consists of two point-like detectors, each measuring the incident far-field irradiance resulting from the thermal source and object combination. The correlation of the two photocurrent outputs isolates the common irradiance fluctuations at their respective transverse locations, yielding information on the mutual coherence function of the effective source created by the true source illuminating the object.

Suppose the baseband envelope of the field incident on detector m , for $m = 1, 2$, is denoted by $E_m(t)$ for $0 < t < T$, having units $\sqrt{\text{photons/s}}$. Because we are considering thermal fields, we assume that the fields have zero mean (i.e., $\langle E_m(t) \rangle = 0$) and a complex degree of coherence

$$\gamma_{1,2}(t-u) \equiv \frac{\langle E_1^*(t)E_2(u) \rangle}{\sqrt{\langle |E_1(t)|^2 \rangle \langle |E_2(u)|^2 \rangle}} \quad (28)$$

that is nonzero. We assume that the coherence time of the two fields (i.e., the time delay τ for which $\langle E_m^*(t+\tau)E_m(t) \rangle$ is appreciable) is equal and given by T_c .

We will carry the following analysis for the photo currents $i_1(t)$ and $i_2(t)$ produced by the detectors in response to the incident optical field. This analysis can be easily generalized for the photon-counting detectors. We have

$$\langle i_m(t) | E_m(t) \rangle = \eta \int d\tau |E_m(\tau)|^2 h_B(t-\tau), \quad (29)$$

and

$$\langle \Delta i_m(t) \Delta i_m(u) | E_m(\cdot) \rangle = \eta \int d\tau |E_m(\tau)|^2 h_B(t-\tau) h_B(u-\tau). \quad (30)$$

Here, $\Delta i(t) \equiv i(t) - \langle i(t) \rangle$, $h_B(t)$ denotes the real-valued baseband impulse response of the photodetectors with time constant (i.e., inverse bandwidth) equal to T_B . With little loss in generality, we assume that $\int dt h_B(t) = 0$, i.e., that the photodetectors are DC blocking, and that $T_B \ll T_c$, i.e., that the coherence time of the source is much longer than the response time constant of the photo detector. Note that the DC term is useful for direct intensity observations, thus it could be tapped off prior to the $h_B(t)$ filter.

The equal-time photocurrent correlation measurement performed at the receiver corresponds to

$$C \equiv \int_0^T dt i_1(t) i_2(t), \quad (31)$$

where C is repeated for every position of the two detectors. Thus, strictly speaking, E_m , i_m and C should have two vector arguments indicating the positions of the two detectors in 2D or 3D space. However, here we are concerned with the SNR at a particular position of these detectors, and therefore we are omitting these variables to avoid clutter. The SNR of the C measurement is defined then as

$$\text{SNR} \equiv \frac{\langle C \rangle}{\sqrt{\langle (C - \langle C \rangle)^2 \rangle}}. \quad (32)$$

Calculating the first and second moments is tedious, but straightforward [11,22]. The SNR can be evaluated, in the $T_c \gg T_B$ limit, as [22]

$$\text{SNR} = \frac{\sqrt{TT_B}}{T_c} \frac{|\gamma_{1,2}|^2 N}{\sqrt{1 + 2N(T_B/T_c) + N^2(T_B/T_c)^2 [|\gamma_{1,2}|^4 + (1 + |\gamma_{1,2}|^2)^2]}}, \quad (33)$$

where $\gamma_{1,2} \equiv \gamma_{1,2}(0)$, and $N \equiv \eta(T_c/T) \int_0^T dt \langle |E_m(t)|^2 \rangle$, for $m = 1, 2$, is the mean photoelectron number per temporal mode (or equivalently per coherence time) of the fields incident on the detectors. The terms in the denominator have intuitive interpretations. The first term, which is independent of N , is due to the shot noise of the two detectors. The third term, with the N^2 dependence, is excess noise resulting from the statistical fluctuations of the incident power on the detectors. This term is sometimes referred to as relative intensity noise. The middle term, with the N dependence, is a result of the beating between the intensity fluctuations and shot noise. In the shot-noise-limited regime, $N \ll 1$ holds, i.e., the mean number of photoelectrons *per mode* is very small, and the SNR can be approximated as

$$\text{SNR} = \frac{\sqrt{TT_B}}{T_c} |\gamma_{1,2}|^2 N. \quad (34)$$

Therefore, the SNR has a linear dependence on the incident photon flux per mode. In the opposite regime with many photoelectrons per mode, thus $N \gg 1$, the SNR saturates to its maximum value

$$\text{SNR} = \sqrt{\frac{T}{T_B}} \frac{|\gamma_{1,2}|^2}{\sqrt{|\gamma_{1,2}|^4 + (1 + |\gamma_{1,2}|^2)^2}}. \quad (35)$$

For direct intensity measurements, we assume that a simple photon bucket operation is performed over T seconds of integration

$$D = \int_0^T dt i(t), \quad (36)$$

where the statistics in Equations (29) and (30) are still true, but we assume that

$\int dt h_B(t) = 1$, such that the DC component is no longer filtered out. Again, defining

$$\text{SNR} \equiv \frac{\langle D \rangle}{\sqrt{\langle (D - \langle D \rangle)^2 \rangle}}, \quad (37)$$

it is straightforward to derive the SNR as

$$\text{SNR} = \sqrt{\frac{T}{T_c} \frac{N}{1 + N}}, \quad (38)$$

where all parameters are as defined before. Thus, when $N \ll 1$, the system is shot-noise-limited and we have

$$\text{SNR} = \sqrt{N \frac{T}{T_c}}, \quad (39)$$

whereas when $N \gg 1$, excess noise dominates and the SNR saturates at

$$\text{SNR} = \sqrt{\frac{T}{T_c}}. \quad (40)$$

To separate the SNR dependence on the integration time T , which is common to both the correlation and direct intensity measurements, it is convenient to normalize it to $\sqrt{T/T_c}$. Figure 10 shows thus normalized SNR of a direct intensity measurement, Equation (38), and the asymptotic approximations, Equations (34) and (35), of a correlation measurement SNRs, as functions of the mean photoelectron number per mode. As seen from this figure, the correlation measurement SNR can approach the direct intensity measurement SNR for the sources with high spectral brightness, $N \approx 1$. The correlation-based measurements typically have worse SNR than direct intensity measurements when shot-noise-limited due to the dependence on the square of the incident average photon number in correlation measurements rather than just the photon number in direct intensity measurements. However, in the excess-noise-limited regime, the correlation measurements' SNR improves due to the fact that such measurements can distinguish source fluctuations from those caused by an object better than the direct intensity measurement. Note, however, these plots compare the SNRs when the photoelectrons per mode are equal in both methods. Whereas correlation-based measurements require that $T_B < T_c$, thereby limiting the total flux incident on the detector, the direct intensity measurement can integrate over a very wide optical bandwidth, without penalty. We have already discussed this aspect of correlation imaging technique in Section II considering the example of solar spectrum.

Thus, in general, the SNR in the correlation measurement is worse than in the direct intensity measurements. Nonetheless, in order to have a realistic assessment of the added value of correlation-based measurements for imaging space objects, one must take into account stray light, detector aging, natural variation of source brightness, and other practical effects that are usually omitted in the SNR analyses published to date. The detectors' dark noise may be particularly important in cases when the incident photons flux is low. On the other hand, the correlation technique may be particularly beneficial for narrow-band imaging, e.g., imaging using a specific spectral line. A narrow spectral feature will lead to the higher spectral brightness and give the correlation imaging advantage according to Figure 10.

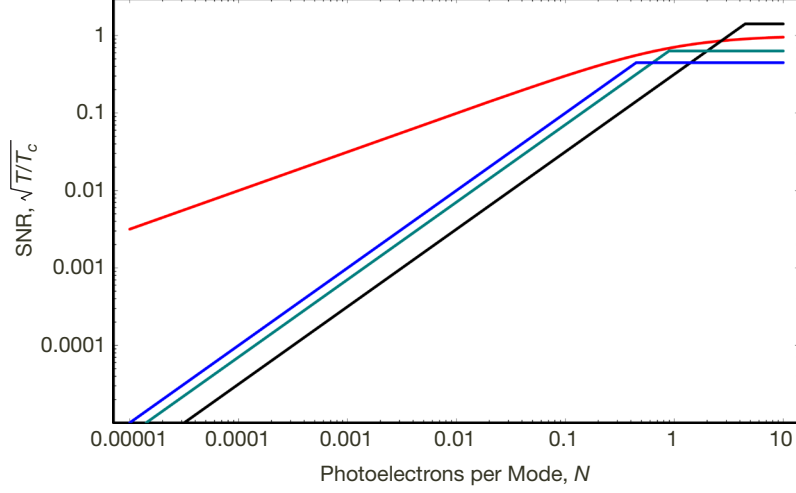


Figure 10. The normalized intensity SNR (red) and correlation measurement SNR for $T_B/T_c = 0.1$ (the lowest), 0.5, and 1.

VI. Conclusions and Summary

We investigate the possibility of performing intensity correlation ghost imaging of dark objects in space illuminated by thermal light sources (stars). Our approach hinges on replacing the beam splitter, indispensable for thermal light ghost imaging but infeasible for space imaging, with the object itself. The absorptive and refractive properties of the object are predicted to imprint themselves on the intensity correlation properties of the transmitted and scattered light and could be extracted from the correlation measurements. To test this concept, we limited our discussion to a fully analytical model relying on a two-dimensional source and an object with Gaussian distribution of luminosity, absorption, or phase delay (the latter representing a thin lens) in paraxial approximation. We demonstrated the variation of the far-field speckle size due to the presence of the object. We have shown that the speckle size variation is a nontrivial function of the object's properties and position. In some cases, it allows us to distinguish different phase and amplitude objects even when they produce very similar shadows and can hardly be distinguished by a direct intensity measurement. Thus, the correlation measurement provides complementary information to a direct observation.

This understanding has encouraged us to apply our analytical model to a realistic space object imaging scenario, such as the Kepler mission. Our prediction for the flux variation is very close to the actual observation. It also predicted a similar (about 10^{-4}) fractional variation of the speckle size. We have carried out a preliminary SNR analysis for a correlation measurement, comparing it to a direct flux measurement. The analysis has shown that, for parameters typical of the Kepler mission, the correlation measurement SNR would be significantly worse than the intensity measurement SNR. This analysis, however, does not include certain instrumental types of noise that may be detrimental for the intensity measurement more than for the correlation measurement and could potentially balance or even reverse the SNR's inequality. These are the dark noise and variation of the detector's responsivity (quantum efficiency) due to environmental fluctuations and aging. The ambi-

ent background light is another important factor that needs to be considered. We plan to include these factors in the advanced noise model, which will be developed in the follow-on research.

Regardless of the technical noises, the correlation measurement SNR improves relative to the intensity measurement SNR when the spectral brightness of the signal increases. Thus, the correlation measurement may be especially advantageous in narrow-band imaging, e.g., imaging based on a selected spectral line. As a final note, comparison of the SNRs of two types of measurement is the decisive criterion when the measurements provide the same type of information. As we have seen, the correlation measurement can provide information additional to the intensity measurement. Moreover, for predominantly phase space objects (such as, e.g., gravitational lenses or dilute gas clouds) producing little or no tell-tale shadows but affecting the optical coherence, correlation ghost imaging may be the preferred option.

Acknowledgments

D.V.S. acknowledges discussions with Drs. Maria Chekhova and Timur Iskhakov.

References

- [1] R. Hanbury Brown and R. Q. Twiss, "Interferometry of the Intensity Fluctuations of Light. I. Basic Theory: The Correlation Between Photons in Coherent Beams of Radiation," *Proceedings of the Royal Society of London A*, vol. 242, no. 1230, pp. 300–324, November 5, 1957.
- [3] I. Klein, M. Guelman, and S. G. Lipson, "Space-Based Intensity Interferometer," *Applied Optics*, vol. 46, issue 20, pp. 4237–4247, June 20, 2007.
- [3] T. B. Pittman, Y. H. Shih, D. V. Strekalov, and A. V. Sergienko, "Optical Imaging by Means of Two-Photon Quantum Entanglement," *Physical Review A*, vol. 52, no. 5, pp. R3429–R3432, November 1995.
- [4] D. V. Strekalov, A. V. Sergienko, D. N. Klyshko, and Y. H. Shih, "Observation of Two-Photon 'Ghost' Interference and Diffraction," *Physical Review Letters*, vol. 74, no. 18, pp. 3600–3603, May 1, 1995.
- [5] K. W. C. Chan, M. N. O'Sullivan, and R. W. Boyd, "Two-Color Ghost Imaging," *Physical Review A*, vol. 79, issue 3, p. 033808, March 9, 2009.
- [6] A. Gatti, E. Brambilla, M. Bache, and L. A. Lugiato, "Correlated Imaging, Quantum and Classical," *Physical Review A*, vol. 70, issue 1, p. 013802, July 6, 2004.
- [7] A. Gatti, E. Brambilla, M. Bache, and L. A. Lugiato, "Ghost Imaging with Thermal Light: Comparing Entanglement and Classical Correlation," *Physical Review Letters*, vol. 93, issue 9, p. 93602, August 27, 2004.
- [8] A. Valencia, G. Scarcelli, M. D'Angelo, and Y. Shih, "Two-Photon Imaging with Thermal Light," *Physical Review Letters*, vol. 94, issue 6, p. 063601, February 16, 2005.

- [9] R. Meyers, K. S. Deacon, and Y. Shih, "Ghost-Imaging Experiment by Measuring Reflected Photons," *Physical Review A*, vol. 77, no. 4, p. 041801(R), April 8, 2008.
- [10] L.-G. Wang, S. Qamar, S.-Y. Zhu, and M. S. Zubairy, "Hanbury Brown–Twiss Effect and Thermal Light Ghost Imaging: A Unified Approach," *Physical Review A*, vol. 79, issue 3, p. 033835, March 24, 2009.
- [11] B. I. Erkmen and J. H. Shapiro, "Ghost Imaging: From Quantum to Classical to Computational," *Advances in Optics and Photonics*, vol. 2, issue 4, pp. 405–450, 2010.
- [12] R. J. Glauber, "The Quantum Theory of Optical Coherence," *Physical Review*, vol. 130, no. 6, pp. 2529–2539, June 1963.
- [13] E. D. Lopaeva and M. V. Chekhova, "Ghost Imaging with the Use of the Variance of the Difference Photocurrent," *Journal of Experimental and Theoretical Physics Letters*, vol. 91, no. 9, pp. 447–451, 2010.
- [14] G. Brida, M. V. Chekhova, G. A. Fornaro, M. Genovese, L. Lopaeva, and I. Ruo Berchera, "Systematic Analysis of Signal-to-Noise Ratio in Bipartite Ghost Imaging with Classical and Quantum Light," *Physical Review A*, vol. 83, issue 6, p. 063807, June 8, 2011.
- [15] T. Iskhakov, A. Allevi, D. A. Kalashnikov, V. G. Sala, M. Takeuchi, M. Bondani, and M. V. Chekhova, "Intensity Correlations of Thermal Light — Noise Reduction Measurements and New Ghost Imaging Protocols," *European Physical Journal Special Topics*, vol. 199, no. 1, pp. 127–138, November 1, 2011.
- [16] National Renewable Energy Laboratory: http://www.nrel.gov/solar_radiation/
- [17] J. G. Cramer, "Generalized Absorber Theory and the Einstein–Podolsky–Rosen Paradox," *Physical Review D*, vol. 22, issue 2, pp. 362–376, July 15, 1980.
- [18] J. G. Cramer, "The Transactional Interpretation of Quantum Mechanics," *Reviews of Modern Physics*, vol. 58, issue 3, pp. 647–687, July–September 1986.
- [19] D. N. Klyshko, "Two-Photon Light: Influence of Filtration and a New Possible EPR Experiment," *Physics Letters A*, vol. 128, issues 3–4, pp. 133–137, 1988.
- [20] J. J. Lissauer, D. C. Fabrycky, E. B. Ford, W. J. Borucki, F. Fressin, et al., "A Closely Packed System of Low-Mass, Low-Density Planets Transiting Kepler-11," *Nature*, vol. 470, no. 7332, pp. 53–58, February 3, 2011.
- [21] F. Fressin, G. Torres, J. F. Rowe, D. Charbonneau, L. A. Rogers, et al., "Two Earth-Sized Planets Orbiting Kepler-20," *Nature*, vol. 482, no. 7384, pp. 195–198, February 9, 2012.
- [22] H. Gamo, "Stellar Intensity Interferometer. I. Signal-to-Noise Ratio for High-Intensity Radiation," *Journal of the Optical Society of America*, vol. 56, issue 4, pp. 441–451, 1966.